MGINS: A Lane-Level Localization System for Challenging Urban Environments Using Magnetic Field Matching/GNSS/INS Fusion

Xiaoji Niu, Longyang Ding, Yan Wang, and Jian Kuang

***Abstract*— Lane-level positioning is a critical technology for supporting assisted driving and autonomous driving applications. However, the Global Navigation Satellite System often falls short in providing reliable positioning (GNSS) due to signal attenuation, obstructions, and multipath in urban areas. Fortunately, typical challenging urban environments, such as tunnels and viaducts, create rich magnetic field features due to abundant ferromagnetic structures, offering an opportunity for magnetic field matching methods to achieve high-precision positioning. This paper presents a novel magnetic field matching/GNSS/Inertial Navigation System (INS) fusion algorithm designed for continuous lane-level positioning in complex environments using cost-effective sensors and computation-saving algorithm. Based on the traditional GNSS/INS tight integration algorithm, this research ensures the performance of the positioning system by enhancing the magnetic field matching and fusion positioning algorithms. First, a coarse-fine magnetic profile matching method is proposed to address the accuracy degradation resulting from the travel distance error of INS-derived trajectory. Second, the magnetic field matching position updates are performed in the vehicle frame, which enables more precise position error modeling. The proposed solution is evaluated through five field tests, covering over 200 kilometers of challenging urban roads. The results demonstrate mean CDF95 position errors of 2.09 m, 1.09 m, and 0.87 m in the forward, lateral, and vertical directions, respectively, and 94.67% accuracy on lane-determination.**

***Index Terms*— Magnetic field matching, low-cost navigation sensors, lane-level positioning, vehicular navigation.**

I. Introduction

THE emergence of Intelligent Transportation System (ITS) has become instrumental in addressing urban traffic congestion and safety concerns. A precise lane-level positioning system is crucial for various ITS applications, including traffic monitoring, vehicle navigation, and fleet management [1]. In complex road networks, navigation systems require lane-level positioning information to assist drivers or autonomous vehicles, especially in heavily congested traffic situations. In numerous autonomous driving or high-precision vehicular positioning systems, various auxiliary sensors, such as odometers, LiDAR, and cameras, are equipped to achieve high position accuracy through data fusion [2], [3], [4], [5], [6]. However, odometers suffer installation and connection hassle, hindering their widespread adoption among the general public. LiDAR, or camera-based solutions, are computationally demanding and susceptible to environmental influences. In contrast, roadside devices like beacons and Ultra-wideband (UWB) technology [7], [8], [9] offer lane-level information but necessitate additional infrastructure, making them less cost-effective and maintenance-friendly for widespread use. Consequently, there is a need for a lane-level positioning system that ensures continuous and accurate positioning in complex urban environments while remaining cost-effective, computation-saving and user-friendly.

In open-sky environments, GNSS technologies, such as Differential GNSS (DGNSS) [5], [10], Real-time Kinematic (RTK), and Precise Point Positioning (PPP) [11], [12], are frequently used alongside lane-level maps to determine the lane. However, in challenging urban environments with dense buildings, tunnels, and underpasses, GNSS technologies experience diminished accuracy or may even become entirely unusable due to multipath and signal obstructions [13]. Hence, the integration of GNSS with other navigation technologies, such as INS, becomes necessary. INS can independently provide accurate relative position, velocity, and attitude information in a short time frame [14]. However, for low-cost Micro-electromechanical Systems (MEMS) Inertial Measurement Units (IMUs), such as those integrated into mobile phones, the INS's position drift quickly reaches several meters within seconds due to biases and high noise. In vehicle navigation, the use of Non-holonomic Constraints (NHC) can significantly enhance the INS's relative positioning capability without incurring additional costs [15]. This enhanced INS, known as the INS-based Vehicle Dead Reckoning (VDR), still faces the challenge of error accumulation over time. Although GNSS is often integrated with VDR to provide continuous and reliable positioning results in vehicle navigation [15], [16], alternative means of absolute positioning are necessary when GNSS signals are blocked.

Magnetic Field Matching (MFM) positioning, as a unique absolute positioning approach, offers stability and incurs zero hardware costs [17], [18]. Notably, areas where GNSS struggles often exhibit prominent magnetic field features. For instance, tunnels, underpasses, viaducts, and urban canyons

Manuscript received 6 November 2023; revised 5 January 2024 and 18 February 2024; accepted 3 April 2024. This work was supported in part by the National Key Research and Development Program of China under Grant 2021YFB2501100, in part by the Hubei Provincial Natural Science Foundation Program under Grant 2023AFB021, in part by the Key Science and Technology Project of Hubei Province under Grant 2022AAA009, and in part by the Fundamental Research Funds for the Central Universities under Grant 2042023kf0124. The Associate Editor for this article was S.-H. Kong.
(Corresponding author: Jian Kuang.)

Xiaoji Niu is with the GNSS Research Center and Hubei Luojia Laboratory, Wuhan University, Wuhan, Hubei 430072, China (e-mail: xjniu@whu.edu.cn).

Longyang Ding, Yan Wang, and Jian Kuang are with the GNSS Research Center, Wuhan University, Wuhan, Hubei 430072, China (e-mail: dingly@whu.edu.cn; wystephen@whu.edu.cn; kuang@whu.edu.cn).
Digital Object Identifier 10.1109/TITS.2024.3386568

contain large steel structures that create magnetic anomalies, resulting in distinctive magnetic fingerprints at each location. This distinctiveness enables high-precision vehicle positioning and lane determination through MFM. Moreover, urban areas with underground railways contribute significant magnetic field features to the road surface. Conversely, regions with less pronounced magnetic field features are typically found on open roads (i.e., open sky), where GNSS observations are more favorable. Evidently, in complex urban environments, regions where GNSS performs poorly align with excellent MFM positioning conditions, while regions with favorable GNSS performance correspond to poorer MFM positioning conditions. Additionally, GNSS is well-suited for initiating MFM, as it requires sequence initialization. All these observations inspire the realization that magnetic field and GNSS serve as two sources of positioning information with excellent complementary properties.

This paper proposes MGINS, an innovative MFM/GNSS/INS fusion algorithm designed to achieve continuous lane-level positioning based on low-cost sensors. The magnetic field plays a key role in determining the lane and the precise vehicle position in regions with intensive buildings and their rich magnetic field features. Building upon the GNSS/INS tight integration algorithm, MGINS effectively harnesses the complementary characteristics between magnetic field and GNSS, demonstrating superior performance in complex environments. The main contributions of this paper are as follows:

- A lane-level positioning solution is implemented using MFM/GNSS/INS through a tightly coupled Extended Kalman Filter (EKF) algorithm. The system effectively fuses MFM positions, single-frequency BDS/GPS raw measurements (pseudo-range and Doppler), MEMS IMU data, and NHC. The system is capable of providing lane-level positioning using very low-cost sensors and limited computation load in complex urban environments, even in challenging areas like viaducts and tunnels, where GNSS signals are heavily obscured or entirely unavailable.
- This study proposes a coarse-fine MFM method that effectively mitigates the matching accuracy degradation caused by travel distance drift without a wheel odometer. Meanwhile, this paper performs MFM position updates in the vehicle frame (v-frame) instead of the navigation frame (n-frame), which fully leverages MFM's ability to distinguish road lanes and enhance the positional accuracy of the MGINS system.

The remainder of this paper is organized as follows: Section II reviews related previous works. Section III provides an overview of MGINS. Section IV and Section V detail the MFM algorithm and multi-sensor fusion algorithm proposed in this paper, respectively. Section VI presents the experimental results and scenario analysis. Finally, we conclude this article and present future work in Section VII.

II. Related Works

GNSS is widely used for providing absolute positioning in outdoor areas and remains the dominant method for automotive navigation systems. Magnetic-field-based positioning techniques have reached maturity in applications like airborne [19] and underwater [20] positioning, and they have been extensively used for indoor positioning in recent years [18], [21], [22]. However, the study of magnetic fields for vehicle positioning is still relatively rare. This section will focus on the state-of-the-art in GNSS and MFM for vehicle positioning.

A. GNSS Positioning

Standard Point Positioning (SPP) services based on GNSS typically offer a positioning accuracy of 2-10 meters [12], [23], which is sufficient for distinguishing roads. Therefore, SPP was initially integrated with commercial road maps for road-level positioning [24], [25]. In [24], a map matching method based on the Hidden Markov Model (HMM) for continuous road-level positioning was proposed. HMM was also employed for smartphone positioning by [25]. With the growing demand for lane-level positioning, relying on SPP and road maps has proven inadequate. Consequently, high-precision GNSS technologies, such as DGNSS, PPP, and RTK, have been utilized with lane-level maps to determine the lane [11], [26]. Although these advanced GNSS positioning techniques significantly improve accuracy, they still have limitations. For example, DGNSS and RTK require the deployment of base stations, while PPP necessitates additional processing. More importantly, all GNSS methods suffer from accuracy degradation and failures in dense urban areas.

B. Vehicle MFM Positioning

MFM positioning has been extensively explored in indoor environments, relying on the distortion of the ambient magnetic field caused by steel structures in buildings. This has inspired researchers to investigate the feasibility of high-precision MFM positioning for outdoor vehicle applications. A study conducted real road experiments in 56 tunnels across two countries over 36 months, achieving positioning accuracy of around 5 meters inside the tunnels [27]. The results verified the temporal stability and regional versatility of magnetic fields within tunnels, supporting the potential for outdoor MFM positioning. Moreover, various factors that could affect the MFM positioning of vehicles were evaluated in [27], including different car types, in-car electronics, and surrounding vehicles. It was found that only semitrailer trucks and metal recycling trucks passing a car had an effect on MFM, which could be easily eliminated by using a sliding average. All other factors mentioned had negligible impacts on MFM. This research demonstrates the reliability of magnetic fingerprinting for vehicle positioning and highlights its potential for use in various outdoor areas. Furthermore, other studies have explored the use of MFM for vehicle location, such as detecting areas with distinct magnetic field features to distinguish lanes [28], determining vehicle location at the road level on multi-layer roads [29], and implementing magnetic field fingerprints in smartphone-based vehicle location systems [30]. However, in areas where magnetic field features are not significant, these methods prove ineffective.

C. Integrated Positioning

GNSS is unreliable in complex urban environments due to its vulnerability. Therefore, to improve the robustness of positioning and the accuracy of lane identification, dead reckoning (DR) based on IMUs or speed sensors is used to assist GNSS for road-level and lane-level positioning [31], [32]. The accuracy of integrated vehicle positioning systems may vary depending on the testing environments and fusion algorithms. Additional sensors have also been integrated with MFM to enhance positioning accuracy and robustness. For example, [33] proposed an odometer-assisted MFM algorithm, achieving an accuracy of 4.8 meters (2σ). The odometer was used to maintain travel distance accuracy, ensuring matching accuracy. However, this scheme relies on additional sensors not present on most mobile phones, making it less accessible for mass users. Additionally, navigation-grade IMU and odometer were employed for DR to assist MFM in [34]. The integrated positioning studies mentioned above are either GNSS-based or magnetic field-based. As for studies on the fusion of magnetic field and GNSS, [35] utilized observations such as on-board diagnostic (OBD) wheel speed, vehicle non-holonomic constraint, and geomagnetic matching to the GNSS/INS loose integration to form a multi-source fusion vehicle navigation system. However, this method requires wheel speed information from OBD, and different vehicle manufacturers do not provide a unified interface. Furthermore, the study did not fully exploit the magnetic field's ability to distinguish between lanes and did not achieve lane-level positioning. In contrast, MGINS does not rely on any speed sensors and achieves lane-level positioning in challenging urban environments.

III. MGINS Overview

The core idea of this work is the development of a lane-level positioning system designed to adapt to complex urban environments by leveraging the complementary properties of the magnetic field and GNSS. The INS-based VDR provides continuous, high-frequency autonomous navigation capabilities. However, VDR is prone to accumulating errors over time, rendering it unsuitable for long-term use. In areas characterized by distinct magnetic field features, such as tunnels, underpasses, and densely built urban areas, these features are harnessed to match the road's magnetic field map, enabling lane-level positioning. The position obtained through MFM serves as a crucial update to correct INS errors. Conversely, in regions with minimal magnetic field features, like open roads, GNSS is relied upon to mitigate the divergence of INS errors and maintain lane-level positioning capabilities.

The block diagram in Figure 1 illustrates the architecture of MGINS, which utilizes an EKF for multi-source information fusion. The MGINS system consists of four primary modules: the VDR module, the MFM module, the GNSS module, and the lane-determination module. The VDR module and the GNSS module incorporate the traditional vehicle GNSS/INS tight integration algorithm. Here the VDR module employs NHC to enhance the relative positioning performance of the INS and serves as the foundational module of MGINS, ensuring continuous availability. The GNSS module utilizes pseudorange and Doppler observations to correct INS errors. Additionally, the GNSS module plays a vital role in initializing the MFM module in open-sky environments.

TABLE I

Description and Definitions of the Coordinate Systems

Symbol	Description	Definition
v-frame	The vehicle frame.	origin: the center of mass of the vehicle. x-axis: pointing to the vehicle's forward direction. y-axis: pointing to the right of the vehicle. z-axis: completing a right-handed orthogonal frame.
n-frame	The navigation frame (i.e., the local level frame).	origin: the same as b-frame. x-axis: towards geodetic north. z-axis: orthogonal to the reference ellipsoid pointing down. y-axis: completing a right-handed orthogonal frame.
b-frame	The body frame (i.e., the coordinate system of the IMU).	origin: IMU measurement center. x-axis, y-axis and z-axis: the IMU's body axes.

The MFM module is the key of MGINS, enabling lane-level positioning. It achieves this by comparing the current observed Magnetic Field Strength (MFS) sequence with a small-scale road magnetic feature map to precisely determine the current vehicle's location. To ensure accurate vehicle positioning, this paper proposes a coarse-fine matching method to deal with the degradation in matching position accuracy caused by the travel distance drift of the VDR. Furthermore, to effectively model the position error during data fusion, this paper proposes performing position updates in the vehicle frame rather than the navigation frame, thereby imposing a smaller constraint variance in the lateral direction and enhancing the localization performance. The definitions of the main coordinate systems involved in this paper are listed in Table I.

Since the MFM module cannot differentiate between lanes in areas with weak magnetic field features, we employ the lane-determination module to achieve continuous lane identification. Specifically, we utilize the road magnetic field map with lane labels as a basic lane-level map, and then project the estimated vehicle positions onto the nearest lanes to determine the current lane. Assuming that the candidate lanes, after trajectory heading filtering, are represented as lane_i, $\boldsymbol{r}^n$ denotes the current estimated vehicle position, and $\overline{\boldsymbol{r}}^n_{ij}$ represents the position of point j on the map of lane_i, the distance from the current vehicle position to lane_i can be approximated as follows:

$$d_{\text{lane}_i} = \min(\|\boldsymbol{r}^n - \overline{\boldsymbol{r}}^n_{ij}\|) \tag{1}$$

Subsequently, the lane with the minimum distance is determined as the final output lane of the MGINS system:

$$l = \arg\min_i (d_{\text{lane}_i}) \tag{2}$$

With the lane determination algorithm clarified, the following sections will delve into the methodologies for obtaining precise vehicle position estimates.

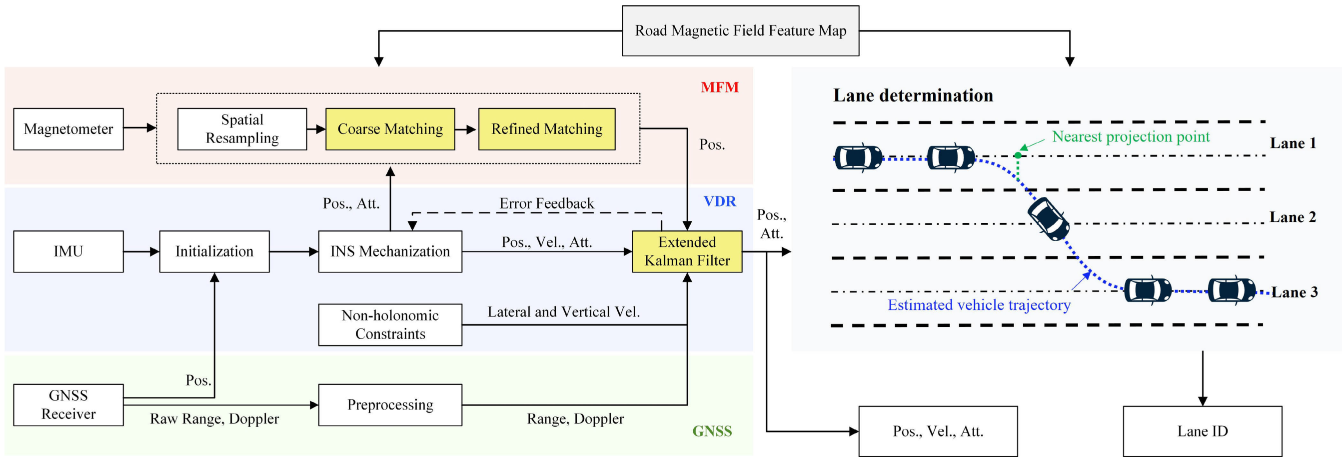

Fig. 1. Block diagram of magnetic field matching/GNSS/INS tightly coupled integration (MGINS).

IV. Magnetic Field Matching Algorithm

The feasibility of outdoor magnetic field matching for localization is attributed to the presence of large steel structures in artificial infrastructures such as tunnels. These structures induce distortions in the ambient magnetic field, resulting in distinctive magnetic fingerprints at each location. Magnetic interference caused by small, moving ferromagnetic objects can be categorized as static or dynamic. For static magnetic interference, such as the vehicle's own metal shell, when the IMU's position relative to the vehicle remains relatively fixed, the impact of the vehicle's ferromagnetic shell on the magnetometer can be equated to the magnetometer bias and eliminated [36]. In the case of dynamic magnetic interference, such as surrounding moving vehicles, the magnetic interference of such a single ferro-object decays rapidly with distance (theoretically cubic times), and its effect is almost negligible when the distance is greater than 1 m [37]. In most scenarios, the distance to the surrounding vehicles is always greater than 1 m for driving safety reasons. The MFM algorithm consists of two phases: road magnetic field feature map generation and real-time positioning.

A. Road Magnetic Field Map Generation

The MFM algorithm in this paper operates in the spatial domain rather than the temporal domain because magnetic field features are spatially related. The road magnetic field map proposed in this paper includes lane identification (ID), lane direction (dir), travel distance (s), magnetic field vector in the n-frame ($\boldsymbol{m}^n$), and position vector ($\boldsymbol{r}^n$). Lane ID distinguishes the lanes, while lane direction provides an estimate based on the vehicle's heading, reducing the number of lane searches during real-time positioning. Magnetic field vectors consist of north, east, and vertical components that are interpolated based on travel distance to corresponding sampling points. By correlating magnetic field vectors with position, a road magnetic field map is generated. The road magnetic field map is organized as a list of continuous track points, and each point contains the following information:

$$\text{Map} = \left\{\text{ID}, \text{dir}, s, \boldsymbol{r}^n, \boldsymbol{m}^n\right\} \tag{3}$$

The road magnetic field map serves as the foundation for implementing the feature matching algorithm. The magnetic field map in this study is measured using a smartphone magnetometer. Furthermore, there are two essential points in its generation: vehicle position determination and magnetometer bias elimination. Vehicle position determination utilizes a high-precision vehicle integrated positioning system, specifically a smoothed Post-processed Kinematic (PPK)/INS/odometer integration method, to achieve positioning accuracy better than 1 dm in complex environments. Magnetometer bias is estimated using the method presented in [38]. Once the accurate vehicle position is obtained and the magnetometer's bias is eliminated, magnetometer measurements can be projected into the north, east, and vertical directions using the attitude. It is worth noting that the road magnetic field map is static data that does not need to be broadcast to the users in real time.

Previous research, such as [27], has verified the feasibility of vehicle MFM and successfully achieved lane-level localization in restricted areas such as tunnels. In this study, we compare magnetic field maps obtained from multiple measurements of the same lane with those from different lanes to briefly validate road MFM positioning and assess map accuracy reliability. Data were collected on Luoyu Road in Wuhan, a typical urban canyon environment. Fig. 2 (a) illustrates the magnetic field maps in the vertical direction generated by passing the same lane three times. It is shown that when passing through the same lane, the high accuracy of the position leads to excellent repeatability in the waveforms of the magnetic field maps produced by three independent measurements. Fig. 2 (b) displays the waveforms of the magnetic field maps in the vertical direction for three adjacent lanes of the road. Noticeably, the magnetic field maps exhibit significant differences across lanes, demonstrating that road magnetic fields can distinguish lanes and provide localization in complex urban environments.

B. Real-Time Positioning

The vehicle's absolute position can be determined by comparing the current magnetic field sequence with the road magnetic field map. In the matching session, accurate travel

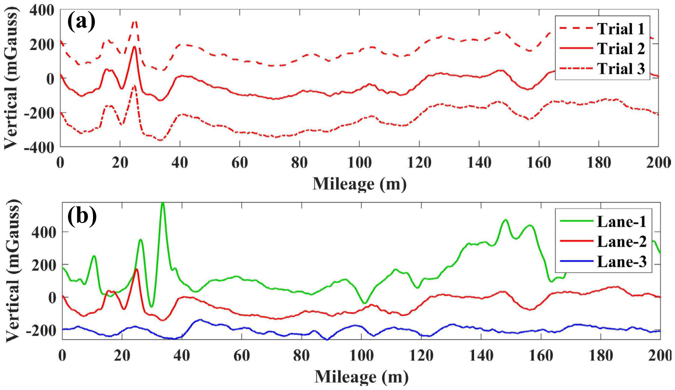

Fig. 2. (a) Repeatability of magnetic field fingerprints in the same lane. (b) Magnetic field fingerprint variations over different lanes.

distance is required when extracting the observed magnetic field sequence in the spatial domain. However, ensuring travel distance accuracy is challenging as this algorithm does not rely on odometers, and GNSS positioning results can be unreliable in complex scenarios. To address this challenge and consider efficiency, we employ Fast Dynamic Time Warping (Fast-DTW) [39] for sequence matching. While Fast-DTW can compress or stretch sequences to achieve optimal matching, it does not directly provide the current optimal matching position (as shown in Fig. 3). Therefore, in this paper, we first use a longer sequence to determine the lane and rough position (coarse matching), followed by a shorter sequence to determine a more accurate position (refined matching), as depicted in Fig. 3. Complete magnetic field matching involves three steps: spatial resampling, coarse matching, and refined matching.

1) Spatial Resampling: As the magnetic field map is based on the spatial domain, the time series of magnetic field data needs to be converted into a spatial series and resampled to align with the magnetic field map's sample rate. To reduce the impact of sensor noise, a 2nd order Butterworth low-pass filter with a cut-off frequency of 5Hz is applied to the magnetometer data, resulting in a smoother magnetic field sequence. Let $\{\boldsymbol{t}, \boldsymbol{m}^b, \boldsymbol{v}^n\}$ represent the smoothed magnetic field and velocity series in the time domain, where $\boldsymbol{t} = (t_1, t_2, \ldots, t_k)$ denotes the time series. $\boldsymbol{m}^b = (\boldsymbol{m}_1^b, \boldsymbol{m}_2^b, \ldots, \boldsymbol{m}_k^b)$ represents the magnetic field series in the body frame (b-frame), and $\boldsymbol{v}^n = (\boldsymbol{r}_1^n, \boldsymbol{r}_2^n, \ldots, \boldsymbol{r}_k^n)$ denotes the velocity series in the n-frame. By employing (4), the time series can be converted to a spatial sequence $\{s, \boldsymbol{m}_b, \boldsymbol{r}^n\}$, where s denotes the travel distance and $\boldsymbol{r}^n$ denotes the position series integrated from the velocity series.

$$\begin{cases} s_k = s_{k-1} + \|\boldsymbol{v}_k^n\|(t_k - t_{k-1}) \\ \boldsymbol{r}_k^n = \boldsymbol{r}_{k-1}^n + \boldsymbol{v}_k^n(t_k - t_{k-1}) \end{cases} \tag{4}$$

Let the entire sequence of magnetic field and position after resampling be $\{\bar{s}, \bar{\boldsymbol{m}}^b, \bar{\boldsymbol{r}}^n\}$, where each element can be represented as:

$$\begin{cases} \bar{s} = (\bar{s}_1, \bar{s}_1 + d, \ldots, \bar{s}_1 + Nd) \\ \bar{\boldsymbol{m}}^b = (\bar{\boldsymbol{m}}_1^b, \bar{\boldsymbol{m}}_2^b, \ldots, \bar{\boldsymbol{m}}_{N+1}^b) \\ \bar{\boldsymbol{r}}^n = (\bar{\boldsymbol{r}}_1^n, \bar{\boldsymbol{r}}_2^n, \ldots, \bar{\boldsymbol{r}}_{N+1}^n) \end{cases} \tag{5}$$

where $(\bar{s}_1, \bar{\boldsymbol{m}}_1^b, \bar{\boldsymbol{r}}_1^n)$ denotes the travel distance, magnetic field, and position of the sequence starting point; d is the spatial sampling distance of the magnetic field map; and N denotes the size of the matching sequence. $(\bar{s}_1 + Nd, \bar{\boldsymbol{m}}_{N+1}^b, \bar{\boldsymbol{r}}_{N+1}^n)$ denotes the travel distance, magnetic field, and position of the sequence endpoint.

Algorithm 1 Coarse Matching Algorithm

Require:
Road magnetic field map M,
Predicted position of the vehicle $\tilde{\boldsymbol{r}}^n$,
Observed MFS sequence after resampling $\{\boldsymbol{m}_{\text{obs}}^b\}$,
Search radius parameter d,
Observed MFS sequence std threshold γ

Ensure:
Coarse matching position p, Lane ID l

if std$(\{\boldsymbol{m}_{\text{obs}}^b\}) > \gamma$ **then**
  Determine candidate lanes based on $\tilde{\boldsymbol{r}}^n$;
  for lane i in M **do**
    Calculate the boundary indexes a and b based on $\tilde{\boldsymbol{r}}^n$ and d_1;
    repeat
      Extract the reference sequence $\boldsymbol{m}_{\text{ref}}^b$ from M;
      Calculate dist$_{ij}$, which is the Fast-DTW similarity distance between the observed MFS sequence and the reference sequence with the position index j on lane i, $j \in [a, b]$;
    until the window slides to the end
    Extract the corresponding position p_i on lane i, $p_i = \arg\min_j(\text{dist}_{ij}),\ j \in [a, b]$;
  end for
  Extract the output lane ID l and the corresponding position index p, $l = \arg\min_i(\text{dist}_{ip})$
end if

2) Coarse Matching: After obtaining the observed sequence in standard format, coarse matching can proceed. For vehicles, the effect caused by ferromagnetic material can usually be equated to the magnetometer bias, which can be considered a constant value over a short period of time. Thus, the algorithm in this paper operates in the b-frame to eliminate the effect of magnetometer bias. To ensure the stability of matching results, both the observed MFS sequence and the reference MFS sequence are de-meaned. Since the reference MFS is in the n-frame, it needs to be projected to the b-frame using the following equation:

$$\boldsymbol{m}_{\text{ref}}^b = \mathbf{C}_n^b \boldsymbol{m}_{\text{ref}}^n \tag{6}$$

where $\mathbf{C}_n^b$ denotes the transformation matrix from the n-frame to the b-frame, and $\boldsymbol{m}_{\text{ref}}^n$ and $\boldsymbol{m}_{\text{ref}}^b$ are the magnetic field vectors before and after projection, respectively. To find the reference sequence that most closely resembles the current observed sequence, the similarity distance between the two sequences needs to be calculated. This paper uses Fast-DTW to calculate the similarity distance. The cost function of Fast-DTW can be expressed as follows:

$$\text{Cost} = \|\boldsymbol{m}_{\text{obs}}^b - \boldsymbol{m}_{\text{ref}}^b\| \tag{7}$$

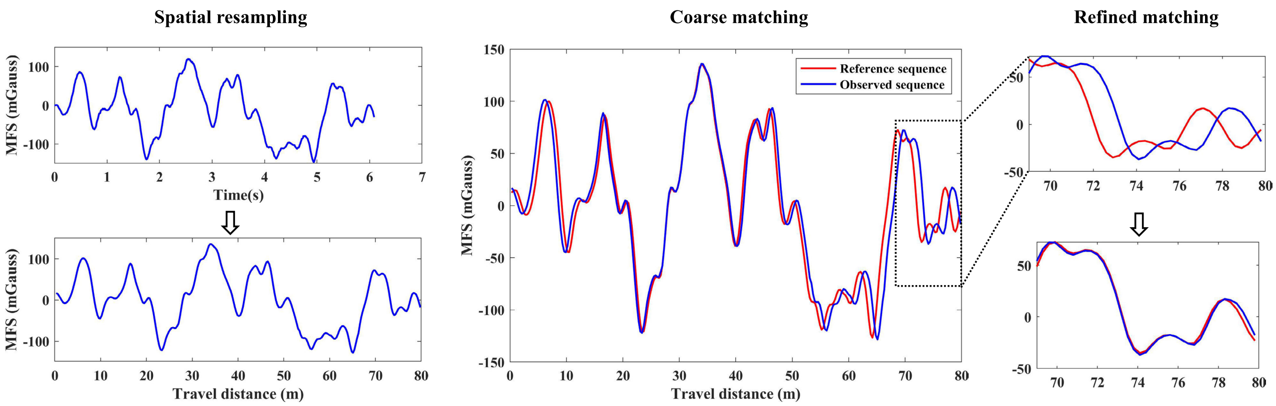

Fig. 3. Scheme of magnetic field sequence matching.

where $\boldsymbol{m}^b = (m_x, m_y, m_z)$ denotes the MFS vector in the b-frame, and the subscripts query and ref denote the observed sequence and the reference sequence, respectively. The coarse matching algorithm is shown in Algorithm 1.

3) Refined Matching: Existing MFM algorithms in the spatial domain typically conclude at the coarse matching step. However, in this paper, we found that sequence matching algorithms such as Fast-DTW cannot directly provide the current optimal matching position in the presence of travel distance error. To fully exploit the potential of MFM localization, we employ a shorter sequence for refined matching to achieve higher accuracy. The processing procedure is similar to the previous one, with the main difference being the use of a shortened sequence length. Additionally, the search range and the threshold settings are adjusted accordingly to accommodate the reduced sequence length. The final matching position of the MFM algorithm in this paper is $(\boldsymbol{r}^n_{\text{ref}})_{l p_{\text{fine}}}$, where p_{fine} can be obtained as:

$$p_{\text{fine}} = \arg\min_j(\text{dist}_{lj}),\ j \in [a', b'] \tag{8}$$

As shown in Fig. 3, while refined matching improves matching accuracy, the reference and observed sequences are still not perfectly aligned due to travel distance error. This problem becomes more evident when the travel distance error increases or when it is in a region with insignificant magnetic field features.

V. Multi-Source Fusion

It is difficult for any single sensor to provide continuous and reliable localization, so multi-sensor fusion is imperative to improve localization performance. The fusion algorithm framework designed in this paper is depicted in Fig. 1.

A. Filter Design

To fuse information from INS, NHC, GNSS, and MFM positions, a tightly coupled EKF is employed. The system state vector is comprised of two key components: the INS error state vector ($\boldsymbol{\delta x}_{\text{ins}}$) and the GNSS clock state vector ($\boldsymbol{x}_{\text{clock}}$) [16], [40]. This can be represented as:

$$\boldsymbol{\delta x} = \begin{bmatrix} \boldsymbol{\delta x}_{\text{ins}} \\ \boldsymbol{x}_{\text{clock}} \end{bmatrix} \tag{9}$$

In real-time vehicle positioning scenarios, IMUs (e.g., mobile phones) are often not fixed in a specific orientation. This renders pre-set mounting angles and NHC lever arms less effective for optimizing NHC performance. To address this, online estimation is used to automatically calibrate the IMU mounting angles and NHC lever arms. Consequently, the state estimation in this paper augments the INS error state vector $\boldsymbol{\delta x}_{\text{ins}}$ with pitch and heading mounting angle errors, along with the NHC lever arm error (3-D). This results in a 26-D INS error state vector, $\boldsymbol{\delta x}_{\text{ins}}$, which can be expressed as:

$$\boldsymbol{\delta x}_{\text{ins}} = [(\boldsymbol{\delta r}^n)^{\text{T}}\ (\boldsymbol{\delta v}^n)^{\text{T}}\ \boldsymbol{\phi}^{\text{T}}\ \boldsymbol{b}_g^{\text{T}}\ \boldsymbol{b}_a^{\text{T}}\ \boldsymbol{s}_g^{\text{T}}\ \boldsymbol{s}_a^{\text{T}}\ (\boldsymbol{\delta\gamma})^{\text{T}}\ (\boldsymbol{\delta l}^b)^{\text{T}}]^{\text{T}} \tag{10}$$

Here, $\boldsymbol{\delta r}^n$ and $\boldsymbol{\delta v}^n$ represent the position error vector and velocity error vector in the n-frame, respectively. Additionally, $\boldsymbol{\phi}$ stands for the attitude error vector, while $\boldsymbol{b}_g$ and $\boldsymbol{b}_a$ signify the bias errors of the gyro and accelerometers, respectively. Moreover, $\boldsymbol{s}_g$ and $\boldsymbol{s}_a$ correspond to gyro and accelerometer residual scale factor errors, and $\boldsymbol{\delta\gamma}$ denotes pitch mounting angle and heading mounting angle errors. Finally, $\boldsymbol{\delta l}^b$ refers to the NHC lever arm error (i.e., the lever arm error from the IMU measurement center to the center of the vehicle's rear wheel). The state error model in continuous form can be expressed as:

$$\begin{cases} \boldsymbol{\delta \dot{r}}^n = -\boldsymbol{\omega}_{en}^n \times \boldsymbol{\delta r}^n + \boldsymbol{\delta\theta} \times \boldsymbol{v}^n + \boldsymbol{\delta v}^n \\ \boldsymbol{\delta \dot{v}}^n = \mathbf{C}_b^n \boldsymbol{\delta f}^b + \mathbf{C}_b^n \boldsymbol{f}^b \times \boldsymbol{\phi} - \left(2\boldsymbol{\omega}_{ie}^n + \boldsymbol{\omega}_{en}^n\right) \times \boldsymbol{\delta v}^n \\ +\boldsymbol{v}^n \times \left(2\boldsymbol{\delta\omega}_{ie}^n + \boldsymbol{\delta\omega}_{en}^n\right) + \boldsymbol{\delta g}_l^n \\ \dot{\boldsymbol{\phi}} = -\boldsymbol{\omega}_{in}^n \times \boldsymbol{\phi} + \boldsymbol{\delta\omega}_{in}^n - \mathbf{C}_b^n \boldsymbol{\delta\omega}_{ib}^b \\ \dot{\boldsymbol{b}}_g = -\dfrac{1}{T_{bg}} \boldsymbol{b}_g + \boldsymbol{w}_{bg} \\ \dot{\boldsymbol{b}}_a = -\dfrac{1}{T_{ba}} \boldsymbol{b}_g + \boldsymbol{w}_{ba} \\ \dot{\boldsymbol{s}}_g = -\dfrac{1}{T_{sg}} \boldsymbol{s}_g + \boldsymbol{w}_{sg} \\ \dot{\boldsymbol{s}}_a = -\dfrac{1}{T_{sa}} \boldsymbol{s}_g + \boldsymbol{w}_{sa} \end{cases} \tag{11}$$

In the above equations, $\boldsymbol{\delta\theta} = \left[\delta\lambda\cos\varphi\ \delta\varphi\ \delta\lambda\sin\varphi\right]^T$, where λ and φ denote the longitude and latitude, respectively; $\delta\lambda$ and $\delta\varphi$ represent the longitude error and latitude error, respectively. $\mathbf{C}_b^n$ is the rotation matrix from the

b-frame to the n-frame, $\boldsymbol{f}^b$ denotes the measurements from the accelerometer, $\boldsymbol{\omega}_{ie}^n$ denotes the angular rate of rotation of the earth in the n-frame, $\boldsymbol{\omega}_{en}^n$ represents the angular velocity of the n-frame with respect to the earth frame (e-frame) resolved in the n-frame, and $\boldsymbol{\omega}_{in}^n$ represents the angular rate of the n-frame relative to the inertial frame (i-frame) in the n-frame. Furthermore, $\boldsymbol{\delta f}^b$ and $\boldsymbol{\delta\omega}_{ib}^b$ denote the sensor errors of accelerometer and gyroscope, which include the bias ($\boldsymbol{b}_g$ and $\boldsymbol{b}_a$) and scale factor ($\boldsymbol{s}_g$ and $\boldsymbol{s}_a$). Both the bias and scale factor are modeled as a first-order Gauss-Markov process, where T and w are the correlation time and drive noise, respectively. A comprehensive explanation of the variables can be found in [40] and [41].

The estimation of the receiver clock error is necessary when employing tightly coupled integration. In this paper, the GNSS clock model consists of two parameters: clock error $\boldsymbol{t}\text{bias}^{\text{sys}}$ and clock drift (denoted by the superscript sys indicating the satellite system). The GNSS clock state vector is given by:

$$\boldsymbol{x}_{\text{clock}} = \left[\boldsymbol{t}_{\text{bias}}^{\text{sys}} \; t_{\text{drift}}\right]^T \tag{12}$$

The clock drift is modeled as a random walk. Consequently, the GNSS clock state model can be expressed as:

$$\begin{aligned} \dot{t}_{\text{bias}}^{\text{sys}} &= t_{\text{drift}} + w_0 \\ \dot{t}_{\text{drift}} &= w_1 \end{aligned} \tag{13}$$

Here, w_0 represents the white noise of the clock error, and w_1 signifies the driven white noise of the random walk.

B. Non-Holonomic Constraint

NHC relies on the motion law of land vehicles, which specifies that a vehicle can predominantly move in the longitudinal direction, while the lateral and vertical velocities are close to zero. NHC has been demonstrated to significantly enhance navigation accuracy and improve the performance of an INS, especially when GNSS signals are obscured. In the v-frame, when NHC holds, the velocity observation vector $\tilde{\boldsymbol{v}}^v$ can be expressed as:

$$\tilde{\boldsymbol{v}}^v = \begin{bmatrix}0 & 0\end{bmatrix}^{\mathrm{T}} + \boldsymbol{\varepsilon}_v \tag{14}$$

Here, $\boldsymbol{\varepsilon}_v$ denotes the observation error, which is determined empirically. Additionally, the projection of the velocity derived from the IMU into the v-frame is expressed as:

$$\begin{aligned} \hat{\boldsymbol{v}}_I^v = \boldsymbol{v}^v + \mathbf{C}_b^v\mathbf{C}_n^b\boldsymbol{\delta v}^n - \mathbf{C}_b^v\mathbf{C}_n^b(\boldsymbol{v}^n\times)\boldsymbol{\phi} + \mathbf{C}_b^v(\boldsymbol{l}^b\times)\boldsymbol{b}_g \\ + (\boldsymbol{v}^v\times)\boldsymbol{\delta\gamma} + \mathbf{C}_b^v(\boldsymbol{\omega}_{ib}^b\times)\boldsymbol{\delta l}^b \end{aligned} \tag{15}$$

Here, $\boldsymbol{v}_I^v$ represents the velocity vector derived from inertial navigation in the v-frame, $\boldsymbol{\omega_{nb}}^b$ denotes the angular velocity of the b-frame with respect to the n-frame resolved in the b-frame, and l_b represents the NHC lever arm (i.e., the distance vector from the IMU center to the center of the vehicle's rear wheel) in the b-frame. Combining (14) and (15) yields the following observation equation:

$$\begin{aligned} \boldsymbol{\delta z}_v = \tilde{\boldsymbol{v}}^v - \hat{\boldsymbol{v}}_I^v = -\mathbf{C}_b^v\mathbf{C}_n^b\boldsymbol{\delta v}^n + \mathbf{C}_b^v\mathbf{C}_n^b(v^n\times)\boldsymbol{\phi} - \mathbf{C}_b^v(\boldsymbol{l}^b\times)\boldsymbol{\delta b}_g \\ - (\boldsymbol{v}^v\times)\boldsymbol{\delta\gamma} - \mathbf{C}_b^v(\boldsymbol{\omega}_{ib}^b\times)\boldsymbol{\delta l}^b + \boldsymbol{\varepsilon}_v \end{aligned} \tag{16}$$

It's worth noting that the algorithm proposed in this paper does not rely on the odometer. Consequently, the vehicle velocity constraint observation equation described above exclusively considers the lateral and vertical components.

C. GNSS Observations Update

The GNSS observations used in this paper consist of pseudorange and Doppler data. The observation equations are written as:

$$\begin{aligned} \tilde{P}_r^s &= \rho_r^s + c\, t_{\text{bias}}^{\text{sys}} + \varepsilon_P \\ \tilde{D}_r^s &= -\frac{1}{\lambda}[\boldsymbol{e}_r^s(\boldsymbol{v}^s - \boldsymbol{v}_r) + c\, t_{\text{drift}} - c\, t_{\text{drift}}^s] + \varepsilon_D \end{aligned} \tag{17}$$

Here, $\tilde{P}$ and $\tilde{D}$ are pseudorange and Doppler observations, respectively, with subscript r indicating the receiver and superscript s indicating the satellite. ρ_r^s is the true range, c signifies the speed of light, and λ represents the carrier wavelength. $\boldsymbol{e}_r^s = \frac{\boldsymbol{r}^s - \boldsymbol{r}_r}{\|\boldsymbol{r}^s - \boldsymbol{r}_r\|}$ signifies the line-of-sight (LOS) unit vector from the receiver to the satellite, where $\boldsymbol{r}^s$ and $\boldsymbol{r}_r$ are the satellite and receiver position vectors, respectively. t_{drift}^s is the satellite clock drift which can be computed by the ephemeris. $\boldsymbol{v}^s$ and $\boldsymbol{v}_r$ denote the satellite and receiver velocity vectors, and ε_P and ε_D represent pseudorange and Doppler observation errors, respectively. The pseudorange and Doppler observations derived from inertial navigation can be expressed as [16] and [40]:

$$\begin{aligned} \hat{\rho}_r^s &= \rho_r^s - \boldsymbol{e}_r^n\boldsymbol{\delta r}^n - \boldsymbol{e}_r^n[(\mathbf{C}_b^n\boldsymbol{l}_G^b)\times]\boldsymbol{\phi} \\ \hat{D}_r^s &= -\frac{1}{\lambda}[\boldsymbol{e}_r^s(\boldsymbol{v}^s - \boldsymbol{v}_r - \boldsymbol{\delta v}_G^n)] \end{aligned} \tag{18}$$

In these equations, $\boldsymbol{l}_G^b$ represents the lever arm from the IMU center to the GNSS antenna in the b-frame. $\boldsymbol{\delta v}_G^n$ represents the IMU velocity error projected to the GNSS antenna in the n-frame, and it can be written as:

$$\begin{aligned} \boldsymbol{\delta v}_G^n = \boldsymbol{\delta v}_I^n - [\mathbf{C}_\omega(\mathbf{C}_b^n\boldsymbol{l}_G^b\times) + (\mathbf{C}_l\boldsymbol{\omega}_{ib}^b\times)]\boldsymbol{\phi} \\ - \mathbf{C}_l b_g - \mathbf{C}_l diag(\boldsymbol{\omega}_{ib}^b)\boldsymbol{s}_g \end{aligned} \tag{19}$$

Here, $\mathbf{C}_\omega$ and $\mathbf{C}_l$ can be expressed as:

$$\begin{aligned} \mathbf{C}_\omega &= (\boldsymbol{\omega}_{ie}^n\times) + (\boldsymbol{\omega}_{en}^n\times) \\ \mathbf{C}_l &= \mathbf{C}_b^n(\boldsymbol{l}_G^b\times) \end{aligned} \tag{20}$$

By combining (17) and (18), we obtain the observation equation for GNSS as follows:

$$\begin{aligned} z_P &= \tilde{P}_r^s - \hat{\rho}_r^s = c\, t_{\text{bias}}^{\text{sys}} + \boldsymbol{e}_r^s\boldsymbol{\delta r}^n + \boldsymbol{e}_r^s[(\mathbf{C}_b^n\boldsymbol{l}_G^b)\times]\boldsymbol{\phi} + \varepsilon_P \\ z_D &= \tilde{D}_r^s - \hat{D}_r^s = -\frac{1}{\lambda}\boldsymbol{e}_r^s[c\, t_{\text{drift}} + \boldsymbol{\delta v}_I^n - [\mathbf{C}_\omega(\mathbf{C}_b^n\boldsymbol{l}_G^b\times) \\ &\quad + (\mathbf{C}_l\omega_{ib}^b\times)]\boldsymbol{\phi} - \mathbf{C}_l\boldsymbol{b}_g - \mathbf{C}_l diag(\boldsymbol{\omega}_{ib}^b)\boldsymbol{s}_g] + \varepsilon_D \end{aligned} \tag{21}$$

In areas with GNSS occlusion or multipath, GNSS observations are susceptible to anomalies. Using a robust Kalman filter can mitigate the impact of outliers, thereby enhancing positioning accuracy and robustness [42], [43]. The Institute of Geodesy and Geophysics III (IGG III) weight function [43] is widely used in robust estimation due to its advantages, including segmentation, continuity, and efficiency. In this paper, IGG III is employed to construct the covariance matrix for the Kalman filter.

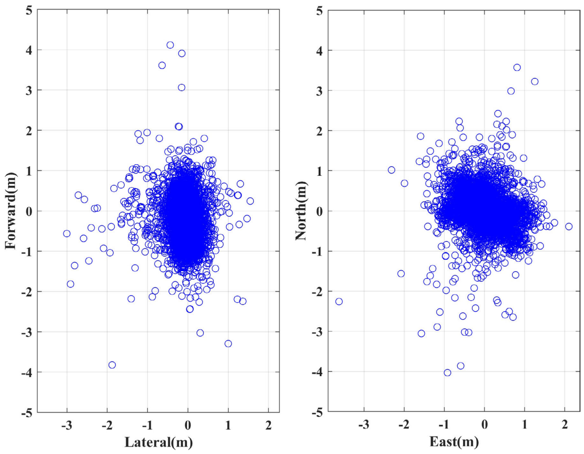

Fig. 4. The magnetic field matching position error resolved in vehicle frame (left) and navigation frame (right), respectively.

Fig. 5. Experimental platforms.

D. MFM Position Update

In challenging scenarios such as urban canyons and tunnels, the magnetic field often exhibits significant features, enabling MFM localization methods to achieve lane-level localization capability. To fully exploit the potential of MFM positioning in the fusion algorithm, a suitable coordinate system needs to be selected to accurately model the position error of MFM. Fig.4 illustrates the MFM position error projected to the v-frame and the n-frame, respectively. The figure reveals that the planar position error of the MFM primarily manifests as forward position error in the v-frame, which is not related to the north and east directions. Therefore, modeling the MFM position error in the v-frame with separate forward and lateral observation noise settings is more aligned with its real error characteristics.

The exact observation vector refers to the difference between the MFM position and the INS position projected in the v-frame, i.e.,

$$z_r = \mathbf{C}_b^v \mathbf{C}_n^b \delta \boldsymbol{r}^n + \boldsymbol{\varepsilon}_{\mathrm{MFM}} \tag{22}$$

Here, $\mathbf{C}_b^v$ denotes the transformation matrix from b-frame to v-frame, determined by the pitch and heading mounting angles of the IMU. $\boldsymbol{\varepsilon}_{\mathrm{MFM}}$ denotes the MFM position error. Ideally, the MFM position error should be adaptive based on the accuracy of the MFM procedure, but it is currently difficult to determine its confidence level. Therefore, the MFM position is modeled as Gaussian white noise with a constant variance, which is determined empirically. To mitigate the impact of outliers, a robust strategy is also employed using IGG III.

VI. Test Results

A. Test Descriptions

To validate the positioning performance of the proposed MGINS scheme, five field tests were conducted in Wuhan. These tests covered three different roads, including various GNSS-challenging environments, such as urban canyons, areas under viaducts, and tunnels. The total length of the test routes amounted to 228 km. The test equipment utilized in the experiments included a low-cost GNSS receiver (ublox-F9P) and a Huawei Mate40 Pro mobile phone. The ublox-F9P provided the single-frequency BDS/GPS pseudorange and Doppler observations, while the Huawei Mate40 Pro supplied 9-axis sensor data (gyroscope, accelerometer, and magnetometer). The ground truth equipment included a navigation-grade IMU (LD-A15, Leador Spatial Information Technology Co., Ltd., China), a professional receiver (Panda, PANDA Space Time Technology Co., Ltd., China), and an odometer. The reference data was achieved through a smoothed PPK/INS/odometer integration method, providing position accuracy ranging from centimeters to a decimeter. The experimental devices and platform are shown in Fig. 5. The ublox-F9P is integrated into the INS-Probe module named H12, which was developed by the Navigation Group, GNSS Research Center, Wuhan University. The odometer was mounted on the left rear wheel of the vehicle, while the mobile phone was mounted in the middle of the vehicle to reduce the impact of electromagnetic interference generated by the engine at the front of the vehicle. Other devices not identified in the figure are not relevant to this paper. The IMU performance parameters of the Huawei Mate40 Pro used in the tests are presented in Table II.

TABLE II
Performance Parameters of the IMU Embedded in Huawei Mate40 Pro

Performance	
Gyroscope bias (deg/h)	200
Angular random walk ($deg/\sqrt{h}$)	3
Accelerometer bias ($mGal$)	1000
Velocity random walk ($m/s/\sqrt{h}$)	1

Detailed information of five tests is provided in Table III. Prior to conducting the tests, the road magnetic field maps for the three roads were established through PPK/INS/odometer processing, ensuring the position accuracy was better than one decimeter. In addition, road magnetic field maps were measured by smartphone magnetometer. The time span between map collection and tests ranged from one day to more than two months. The resolution of the magnetic feature maps is set to 0.5 meters. Fig. 6 shows the three roads where

TABLE III
DETAILED INFORMATION OF FIVE TESTS

Test	Road	Scenarios*	Time span (day)	Average speed (m/s)	Travel distance (km)
1	A	**a**, **c**	67	20.5	19.9
2	B	**a**, **b**, **c**, **d**, **e**	2	21.5	38.4
3	B	**a**, **b**, **c**, **d**, **e**	2	20.6	38.4
4	C	**c**, **d**, **e**	1	50.3	65.9
5	C	**c**, **d**, **e**	1	47.0	65.8
		Total			≈228

* **a**, urban canyon; **b**, tunnel; **c**, under a viaduct; **d**, on a viaduct; **e**, open road.

TABLE IV
CONDITION SETTINGS OF MFM-1, MFM-2, AND MFM-3

Algorithms	Matching Methods	Magnetometer Bias Elimination
MFM-1	Coarse Matching	Differential MFS in the b-frame
MFM-2	Coarse-fine Matching	Differential MFS in the n-frame
MFM-3	Coarse-fine Matching	Differential MFS in the b-frame

the tests were conducted, with the blue lines indicating the test tracks. Embedded within the figure are photographs of the surroundings taken along the route. During the tests, the vehicle circled normally along the test roads without deliberate lane changes. Each road consisted of 1–3 lanes. Road A, situated on Luoyu Road, represents a typical urban canyon environment, characterized by high buildings on both sides of the road. Road B, located on Wuluo Road, is the typical challenging environment for GNSS, encompassing the Fruit Lake Tunnel, areas under the viaduct, regions flanked by high buildings, and normal open roads. Road C is situated on the Guanggu Avenue Viaduct, encompassing both open viaduct roads and heavily obscured underpasses. Five tests were carried out as follows: Test 1 on Road A, Test 2 and 3 on Road B, and Test 4 and 5 on Road C. Additionally, Tests 1, 2, and 3 experienced traffic jams, while Tests 4 and 5 saw smoother vehicle travel conditions.

B. MFM Positioning Performance

This section is dedicated to evaluating and comparing the performance of the MFM algorithms. We have chosen Test 5 as the evaluation dataset due to the rich magnetic field features along the viaduct road. The MFM is initialized by GNSS in open-sky. The condition settings of the MFM algorithms to be compared are given in Table IV. Specifically, MFM-3 represents the complete MFM algorithm as described in Section IV. In contrast, MFM-1 and MFM-2 are its simplified versions. In comparison to MFM-3, MFM-1 simplifies the matching algorithm to coarse matching. On the other hand, MFM-2 uses the differential MFS in the n-frame to eliminate the effect of magnetometer bias. These variations in the MFM algorithms will be assessed to evaluate their impact on positioning performance in Test 5.

Table V provides the matching position errors (CDF68 and CDF95) for three MFM algorithms, and the Probability Density Function (PDF) curves corresponding to the forward and lateral position errors are illustrated in Fig. 4. Table VI

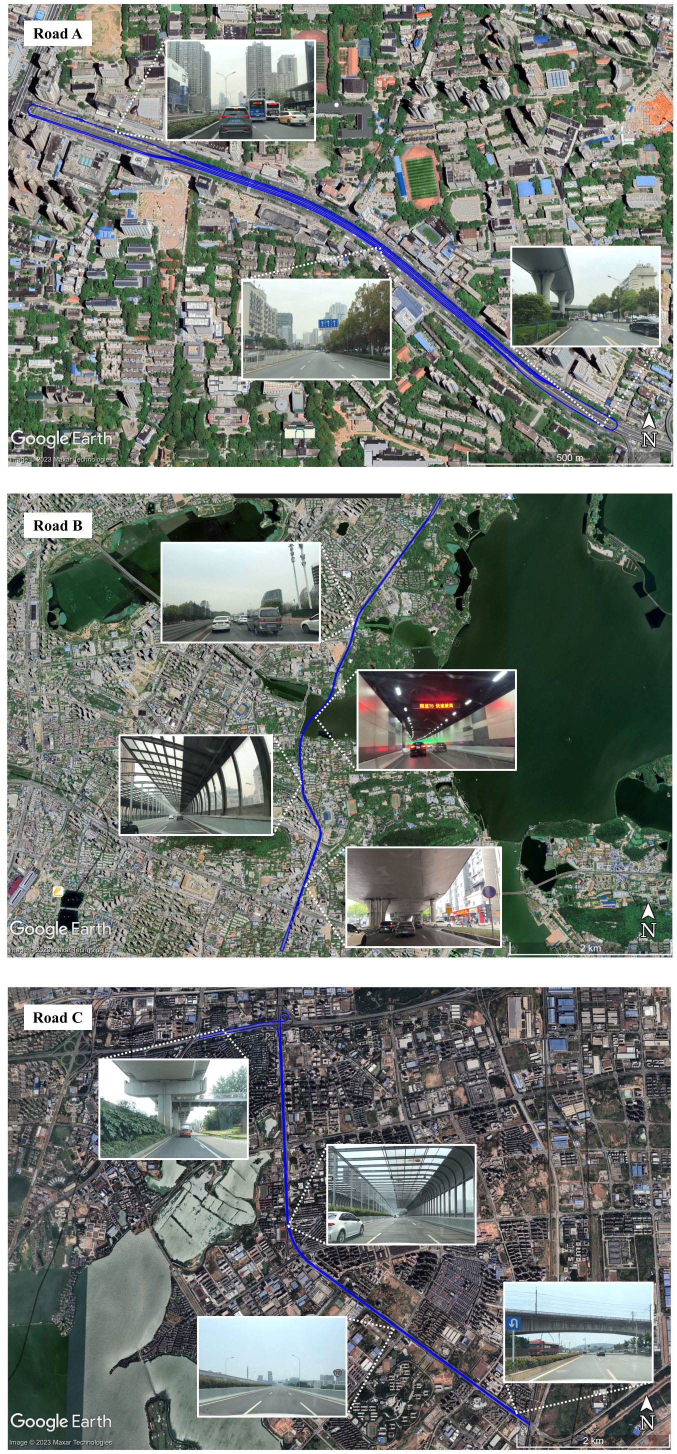

Fig. 6. Test trajectory (from Google Earth) and environment on three roads.

describes how the metrics involved in this paper are defined. It is worth mentioning that Cumulative Distribution Function (CDF) is the integral of PDF.

Since the algorithm in this paper does not rely on the odometer, achieving a stable and continuous position update can be challenging, especially when significant magnetic field features are not consistently available in real-world environments. Consequently, eliminating travel distance error becomes a complex task. A large travel distance error can

TABLE V
POSITION ERRORS OF MFM-1, MFM-2, MFM-3

Methods	Position error (m)					
	CDF68			CDF95		
	Forward	Lateral	Vertical	Forward	Lateral	Vertical
MFM-1	1.30	0.37	0.30	876.27*	84.33*	32.27*
MFM-2	0.61	0.23	0.23	1.24	0.75	0.40
MFM-3	0.61	0.23	0.22	1.21	0.74	0.40

* denotes the matching results diverge due to travel distance drift.

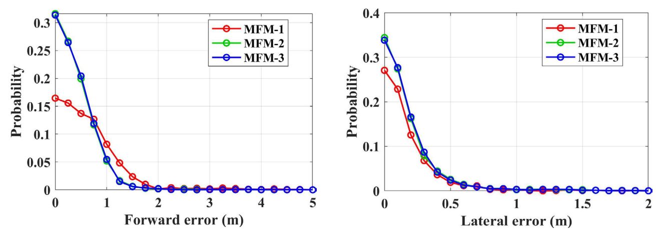

Fig. 7. Probability density function curves of positioning errors for three magnetic field matching methods.

TABLE VI
PERFORMANCE EVALUATION METRICS DEFINITIONS

Metric	Descriptions
MAX	Maximum of the absolute value of the positioning error.
CDF68	Positioning error value corresponding to the cumulative distribution function with 68% in one test.
CDF95	Positioning error value corresponding to the cumulative distribution function with 95% in one test.
Lane-determination accuracy	Proportion of epochs with correct lane-determination.
Forward/Lateral/ Vertical position error	The forward, lateral and vertical directions of the positioning errors resolved in the vehicle frame, respectively.

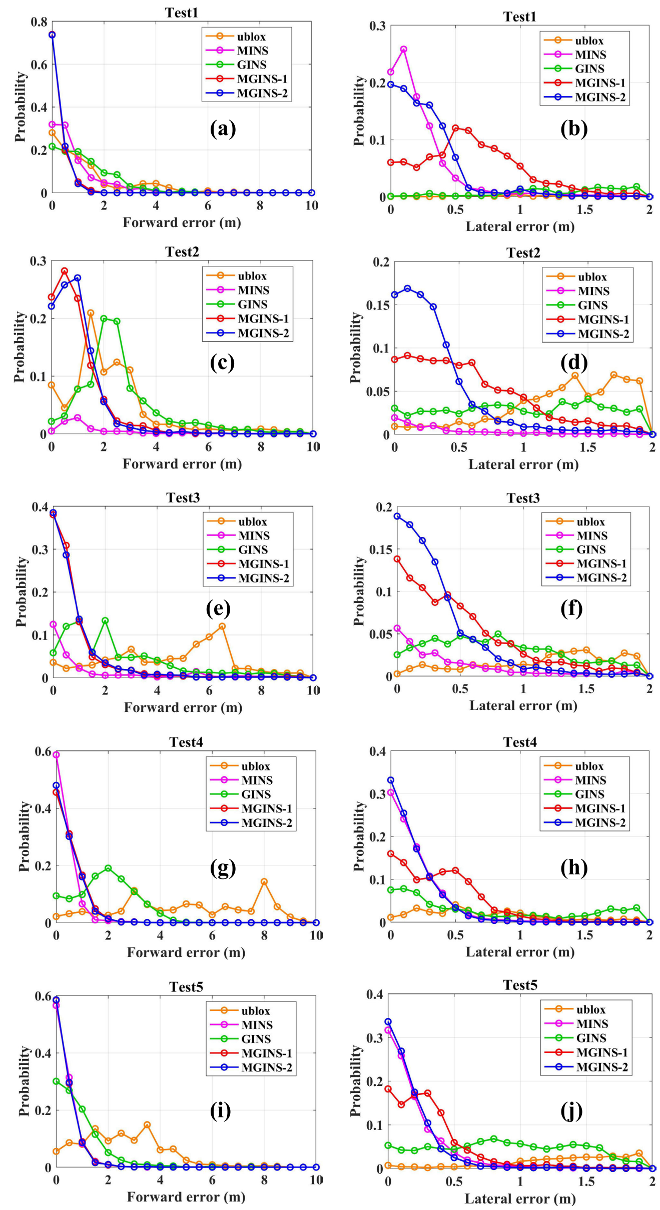

Fig. 8. Probability density function curves of positioning errors for five positioning schemes over 5 tests. The left and right figures represent the forward and lateral positional error respectively.

lead to significant position errors, ultimately causing filter divergence and rendering the travel distance drift completely uncontrollable. This is the reason for the failure of the MFM-1 method in the latter part of the evaluation. In contrast, the coarse-fine matching method is more effective in mitigating position errors caused by travel distance error. It can provide stable and accurate position observations, resulting in higher accuracy and robustness.

Comparing MFM-2 and MFM-3, it can be found that the effect of magnetometer bias can also be effectively eliminated using differential MFS in the n-frame (MFM-2) as well as in the b-frame (MFM-3), which is quite different from the conclusion in our previously published work on pedestrian MFM positioning [44]. This is primarily because, for the majority of the test duration, the vehicle's attitude changes are minimal within the length of the matching window (80 meters in this study). Consequently, the magnetometer bias has little impact on the MFM-2 method during most of the test. However, it is worth noting that when the magnetometer attitude fluctuates significantly within the length of the matching window, the differential MFS in the n-frame (MFM-2) cannot completely eliminate the effect of magnetometer bias anymore. In contrast, the differential MFS in the b-frame (MFM-3) used in this paper remains unaffected.

C. Multi-Source Fusion Positioning Performance

This section focuses on evaluating the positioning accuracy of the five schemes, with the magnetic field-based schemes using the MFM-3 algorithm discussed in the previous section:

- **ublox**, which gives SPP results based on dual-frequency observations directly provided by the commercial receiver ublox-F9P.
- **MINS**, initialized by GNSS alone, with subsequent INS error correction using MFM positions and NHC, as described in Sections V-B and V-D.

TABLE VII
PERFORMANCE STATISTICS OF UBLOX, MINS, GINS, MGINS-1 AND MGINS-2 IN 5 TESTS

Scheme	Test	Position error (m)									Lane-determination accuracy (%)
		MAX			CDF68			CDF95			
		Forward	Lateral	Vertical	Forward	Lateral	Vertical	Forward	Lateral	Vertical	
ublox	1	8.08	8.52	16.11	1.59	6.63	9.87	4.49	7.92	13.04	75.00
	2	924.16	1253.67	106.52	3.14	2.03	5.83	54.40	19.22	13.87	66.00
	3	877.13	518.33	293.17	6.78	3.66	13.17	73.88	25.66	40.59	61.53
	4	14.16	12.68	18.28	7.19	6.09	10.06	9.07	7.29	12.92	67.91
	5	9.58	9.10	11.93	3.58	3.67	8.04	5.26	4.89	9.78	30.01
	Mean	**366.62**	**360.46**	**89.20**	**4.46**	**4.42**	**9.39**	**29.42**	**13.00**	**18.04**	**60.09**
MINS	1	14.71	17.78	3.28	1.13	0.32	0.21	3.28	2.61	0.70	92.78
	2 *	3210.98	3087.09	333.19	2708.36	723.80	165.44	3022.34	2040.65	234.59	1.97
	3 *	782.64	786.23	242.70	117.13	488.16	145.52	287.76	587.58	192.92	14.24
	4	56.97	15.46	5.34	0.60	0.27	0.34	1.28	0.74	0.76	96.14
	5	6.68	2.61	2.00	0.64	0.26	0.32	1.30	0.72	0.64	96.27
	Mean	**814.40**	**781.83**	**117.30**	**565.57**	**242.56**	**62.37**	**663.19**	**526.46**	**85.92**	**60.28**
GINS	1	5.89	5.87	13.12	1.76	3.69	3.87	3.38	4.72	10.16	76.98
	2	108.79	62.28	20.46	3.32	2.24	3.57	52.47	19.25	10.67	61.47
	3	88.52	48.12	22.66	4.61	3.14	4.33	30.95	24.91	11.17	66.06
	4	6.75	7.50	8.80	2.71	2.25	4.00	3.96	3.21	5.89	72.34
	5	8.96	8.83	6.16	1.28	1.30	2.38	2.64	2.32	3.96	84.16
	Mean	**43.78**	**26.52**	**14.24**	**2.74**	**2.52**	**3.63**	**18.68**	**10.88**	**8.37**	**72.20**
MGINS-1	1	2.09	4.00	1.80	0.43	0.83	0.27	1.06	1.56	0.70	94.42
	2	9.74	4.58	1.88	1.27	0.83	0.34	2.76	2.41	0.91	88.31
	3	18.65	5.49	2.13	1.02	0.67	0.33	4.57	1.90	0.80	90.25
	4	3.92	2.81	2.01	0.84	0.56	0.40	1.60	1.02	1.03	97.28
	5	5.55	2.70	2.42	0.62	0.40	0.53	1.28	1.03	0.97	96.38
	Mean	**7.99**	**3.92**	**2.05**	**0.84**	**0.66**	**0.37**	**2.25**	**1.58**	**0.88**	**93.33**
MGINS-2	1	2.05	3.24	2.97	0.43	0.38	0.29	0.98	1.09	0.70	95.90
	2	11.72	4.11	1.87	1.38	0.43	0.34	2.44	1.94	0.91	91.64
	3	20.56	3.58	2.11	1.08	0.41	0.33	4.22	1.27	0.74	91.64
	4	3.94	2.23	2.02	0.80	0.25	0.41	1.57	0.55	1.03	97.68
	5	5.68	2.13	2.41	0.62	0.23	0.54	1.25	0.59	0.98	96.47
	Mean	**8.79**	**3.06**	**2.28**	**0.86**	**0.34**	**0.38**	**2.09**	**1.09**	**0.87**	**94.67**

* denotes the MINS scheme diverges, leading to VDR standalone solution in these tests.

- **GINS**, which utilizes single-frequency BDS/GPS raw measurements (pseudorange and Doppler) along with NHC to correct INS errors, as described in Sections V-B and V-C.
- **MGINS**, the algorithm proposed in this paper, which fuses NHC, single-frequency BDS/GPS raw measurements (pseudorange and Doppler), and MFM position observations using the method described in Section V. To assess the impact of the v-frame-based position updates proposed in this paper, the MGINS scheme was further divided into **MGINS-1** and **MGINS-2**, whose difference lies in the choice of coordinate frame for position updates: MGINS-1 employs the n-frame, while MGINS-2 utilizes the v-frame.

To quantitatively evaluate the lane-level positioning performance of various positioning schemes, we apply the identical lane determination method used in the MGINS scheme to acquire lane labels for the other positioning schemes. Lane label truths are derived by associating position truths with lane maps (road magnetic field maps). Subsequently, these truths are compared with the observed lane labels to determine the accuracy of lane identification. Unmapped areas, such as intersections, are excluded from the lane determination accuracy calculations.

Figure 8 illustrates the probility density function of the forward and lateral positioning errors for the five schemes across five tests, respectively. Table VII provides information on the MAX, CDF68, CDF95, and lane-determination accuracy for the five schemes across the five tests. The results indicate that the average lane-determination accuracy for the ublox, MINS, GINS, MGINS-1, and MGINS-2 solutions are 60.09%, 60.28%, 72.20%, 93.33%, and 94.67%, respectively. Among these, MGINS-2 consistently achieves over 90% lane-determination success rate in all five tests. The mean CDF95 position errors for MGINS-2 are 2.09 m, 1.09 m, and 0.87 m in the forward, lateral, and vertical directions, respectively. A comparison of the statistical results for the five schemes yields the following insights:

1) Comparison of MGINS-2, ublox, and GINS Schemes: With the addition of INS and NHC, GINS outperforms ublox in GNSS-denied road sections such as tunnels (Tests 2 and 3), reducing the maximum error from around 1 km to around 100 m. Over the five tests, MGINS-2 outperforms GINS in almost all evaluation metrics. This improvement is attributed to the utilization of the magnetic field, which provides accurate lane constraints for the vehicle's lateral position and offers higher accuracy in forward position constraints based on the coarse-fine matching method proposed in this paper.

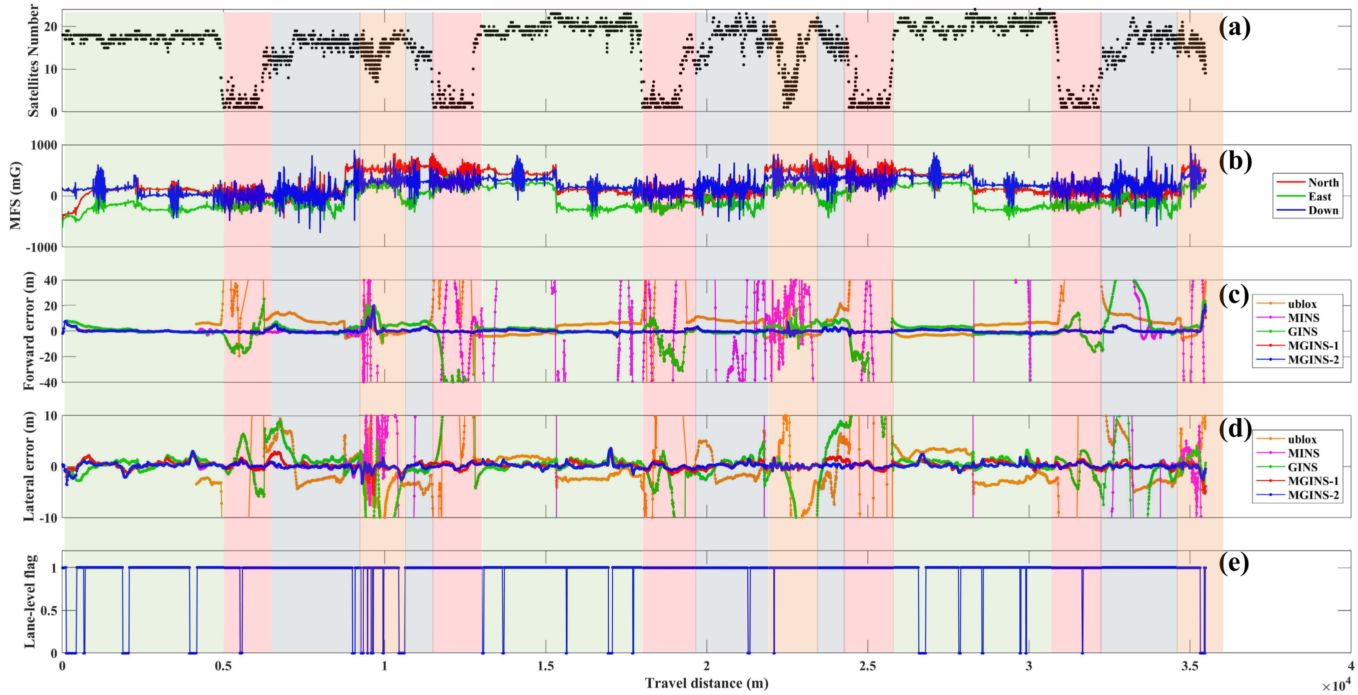

Fig. 9. Analysis of five positioning schemes in Test 3. The red shaded area represents passing through tunnels, the yellow shaded area represents passing under viaducts, the green shaded area indicates passing through a normal open road, and the rest of the area represents the other sections of the road, such as urban canyons marked with blue. (a) The number of satellites. (b) The magnetic field strength sequence measured by smartphones. (c) The forward error of five schemes. (d) The lateral error of five schemes. (e) The lane-level positioning flag of MGINS-2: 1 indicates successful lane-determination, and 0 means failure.

2) Comparison of MGINS-2 and MINS Schemes: In Road A (Test 1) and Road C (Test 4 and Test 5), both MINS and MGINS-2 show stable positioning performance, primarily due to the consistent presence of significant magnetic field features in these tests. For example, Road C is a viaduct with substantial steel materials, resulting in prominent magnetic field features. Consequently, both MINS and MGINS-2 achieve more than 95% lane-determination accuracy on this road. In Road B (Test 2 and Test 3), MGINS-2 shows significant improvement over MINS in all evaluation metrics. MGINS-2 demonstrates higher positioning accuracy compared to MINS, mainly for the following reasons:

- In areas with weak magnetic field features, the MINS matching position errors could increase, and the MINS scheme might even fail, while MGINS-2 utilizes GNSS to ensure positioning accuracy in these regions.
- GNSS provides velocity constraints on open roads, ensuring travel distance accuracy and yielding more precise MFM positions.
- Since the road magnetic field map does not cover intersections, MINS automatically degrades to a VDR scheme once reaching the end of the road until an effective MFM position update is regained. In contrast, MGINS-2 uses GNSS to correct INS errors in these unmapped areas.

3) Comparison of MGINS-2 and MGINS-1 Schemes: The results indicates that the MGINS-2 scheme exhibits improved lateral position accuracy compared to the MGINS-1 scheme, with no significant change in forward and vertical position accuracy. Specifically, the mean CDF68 lateral position error decreases from 0.66 m to 0.34 m, and the mean CDF95 lateral position error decreases from 1.58 m to 1.09 m. This improvement can be attributed to the fact that the error characteristics of the MFM are primarily associated with the v-frame rather than the n-frame. Consequently, performing position updates in the v-frame allows for a more precise modeling of position errors, thereby improving lateral positioning accuracy.

D. Scenario Analysis

This section selects Test 3 as a representative case for a comprehensive comparison and analysis of the performance of the five positioning schemes. Fig. 9 provides a comprehensive overview of Test 3, including the number of visible satellites from the ublox-F9P receiver, the magnetic field sequences measured by smartphones, the forward position error sequences, the lateral position error sequences, and the lane-level positioning flag for the MGINS-2 scheme. Different road sections, such as tunnels, under-viaducts, normal open roads, and others, are color-marked for clarity. To eliminate the effects of velocity, the information in Fig. 9 has been transformed into a function of travel distance rather than time. Fig. 10 displays the trajectories of the five schemes in Test 3.

Based on the data presented in Fig. 9 and Fig. 10, MGINS-2 demonstrates clear advantages over the other four schemes. The ublox scheme experiences significant accuracy degradation, and in challenging urban environments such as tunnels and under-viaduct roads, it can become almost unusable due to GNSS limitations. This highlights the vulnerability of GNSS in complex urban settings. Compared to ublox, GINS is able to provide continuous and stable positioning. However, in areas where GNSS is unavailable (e.g., tunnels), GINS degrades

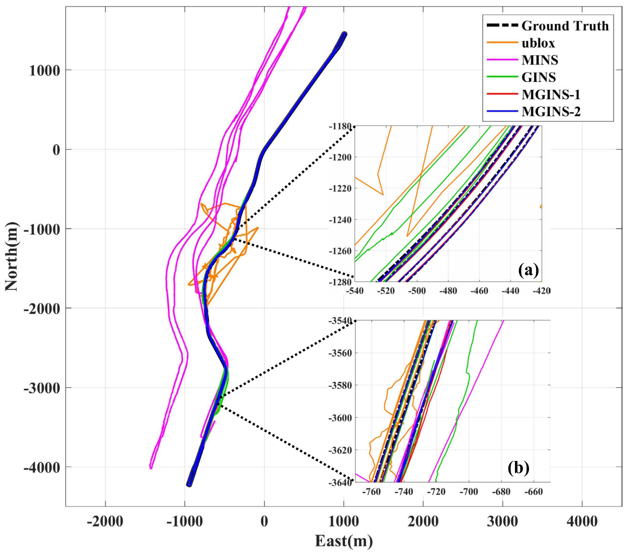

Fig. 10. Trajectory comparison of Test 3. (a) Inside the tunnel. (b) Under the viaduct.

to a VDR solution, which suffers from error accumulation and can't meet lane-level positioning requirements. The MINS scheme initially achieves accurate positioning using the MFM algorithm when strong magnetic field features were present. However, in prolonged sections with weak magnetic field features, the MFM position error increases, leading to a degradation in travel distance accuracy, resulting in the trajectory deviating from the road.

Fig. 11 provides specific details of tunnel, under-viaduct, and open road sections extracted from Fig. 9. The following information can be obtained:

1) Tunnel Scenario: In the tunnel scenario (Fig. 11 (a)), the number of visible satellites is nearly zero. Therefore, in tunnels, the MGINS scheme is almost equivalent to the MINS scheme, relying on rich magnetic field features to obtain continuous and accurate position updates.

2) Under-Viaduct Scenario: In the under-viaduct scenario (Fig. 11 (b)), significant magnetic field features are present, and the number of visible satellites is around 5-10, with many gross errors. Both ublox and GINS are notably affected by this condition, resulting in position errors of 20-30 meters. It remains challenging for us to completely eliminate the impact of gross GNSS errors in such scenarios. Consequently, the MGINS-2 scheme was also influenced by GNSS outliers at times, leading to a maximum position error of around 20 meters.

3) Normal Open Road Scenario: In the normal open road scenario (Fig. 11 (c)), the magnetic field features are weak, and the differences in magnetic field features between lanes are not distinct enough, leading to more lane misclassifications compared to the tunnel scenario. Consequently, the lane-determination accuracy decreases. However, despite the weak magnetic field features in this road section, the GNSS observation conditions are good, ensuring both positioning and travel distance accuracy. Therefore, even with a small number of magnetic field features, the MGINS-2 scheme can still fully utilize them to achieve lane-level positioning in most areas.

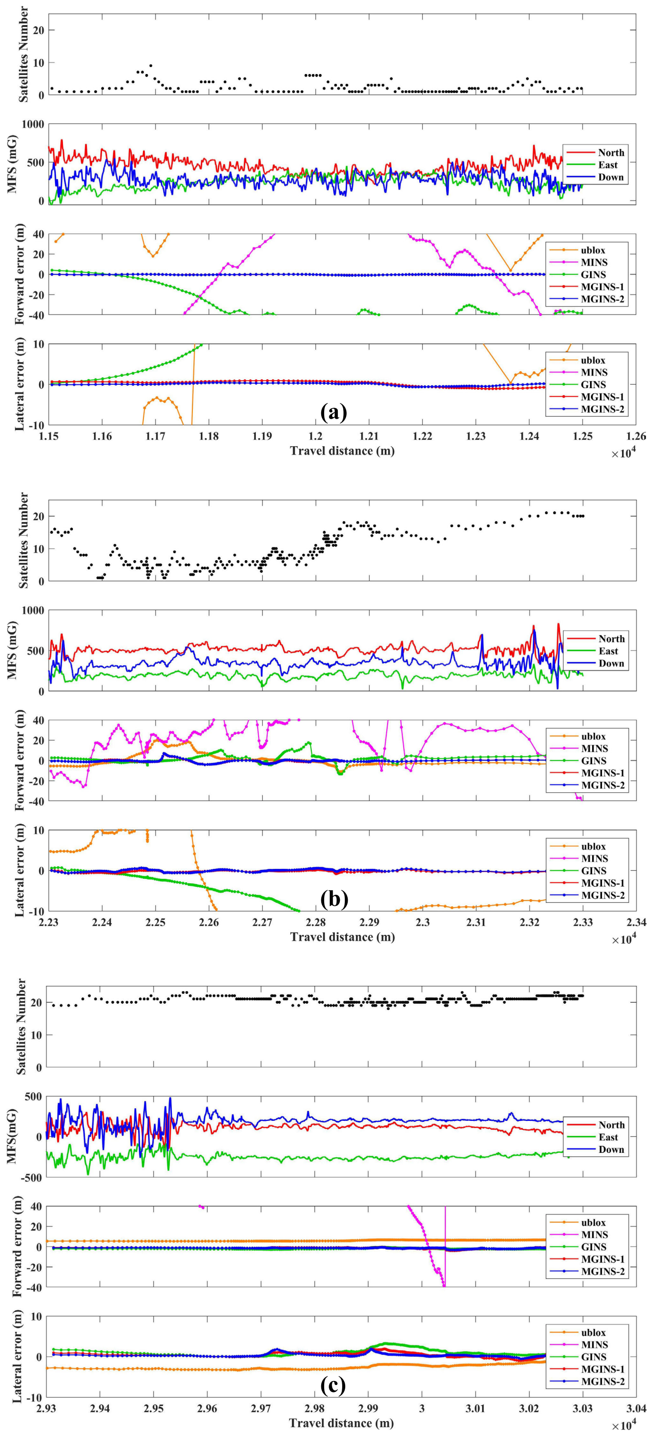

Fig. 11. (a) Tunnel Scenario. (b) Under Viaduct Scenario. (c) Normal Open Road Scenario.

In summary, GNSS and magnetic field features demonstrate significant complementarity in complex urban environments. However, the impact of GNSS gross errors under the viaduct and the weak magnetic field features of the normal open road may lead to some degradation on the accuracy of the MGINS-2 scheme.

VII. Conclusion and Future Work

This study presents a lane-level localization system that integrates magnetic field matching (MFM), GNSS, and INS for challenging urban environments. It delivers lane-level positioning accuracy through MFM in GNSS-challenging scenarios like tunnels and under viaducts and maintains lane-level positioning accuracy through GNSS and NHC in open road scenarios. To enhance the positioning accuracy and robustness of the proposed MGINS, the following optimizations are implemented in this paper:

- To address the issue of matching accuracy degradation caused by the travel distance drift of the INS (i.e. VDR) trajectory, a coarse-fine matching method is proposed. Experimental results demonstrate that the CDF68 position errors of MFM in this paper reach 0.61 m, 0.23 m, and 0.22 m in the forward, lateral, and vertical directions, respectively, representing error reductions of 53%, 38%, and 27% compared to the coarse matching method.
- To accurately model the MFM position error in the integrated positioning algorithm, this paper proposes performing MFM position updates in the v-frame instead of the n-frame. Experimental results showed that this approach reduces the mean lateral CDF68 position error from 0.66 m to 0.34 m.

Five tests were conducted to evaluate the accuracy of the proposed MGINS. In comparison to peer solutions, including ublox, MFM/INS (MINS), and GNSS/INS (GINS), the MGINS scheme demonstrates significant advantages, achieving the highest positioning accuracy and the best robustness. The mean CDF95 position errors in the forward, lateral, and down directions are 2.09 m, 1.09 m, and 0.87 m, respectively, with a mean lane-determination accuracy of 94.67%. Furthermore, a comprehensive test, including different scenarios (e.g., tunnels, under-viaducts, and ordinary roads), is investigated in detail, and the factors affecting the positioning accuracy of MGINS are discussed comprehensively.

The magnetic field map serves as the foundation for the proposed feature matching algorithm, and future research should focus on obtaining the magnetic field map more efficiently and cost-effectively, such as through crowdsourcing. Moreover, since not all regions have sufficient magnetic field features, the matching window length of the MFM algorithm should adapt to the distribution of the magnetic field in the region. Additionally, some measures should be taken to detect the gross errors of MFM and GNSS, further enhancing positioning accuracy and robustness.

References

[1] J. Du and M. J. Barth, "Next-generation automated vehicle location systems: Positioning at the lane level," *IEEE Trans. Intell. Transp. Syst.*, vol. 9, no. 1, pp. 48–57, Mar. 2008.

[2] J. Tang et al., "LiDAR scan matching aided inertial navigation system in GNSS-denied environments," *Sensors*, vol. 15, no. 7, pp. 16710–16728, Jul. 2015.

[3] G. Hemann, S. Singh, and M. Kaess, "Long-range GPS-denied aerial inertial navigation with LiDAR localization," in *Proc. IEEE/RSJ Int. Conf. Intell. Robots Syst. (IROS)*, Oct. 2016, pp. 1659–1666.

[4] T. Li, H. Zhang, Z. Gao, X. Niu, and N. El-sheimy, "Tight fusion of a monocular camera, MEMS-IMU, and single-frequency multi-GNSS RTK for precise navigation in GNSS-challenged environments," *Remote Sens.*, vol. 11, no. 6, p. 610, Mar. 2019.

[5] A. Vu, A. Ramanandan, A. Chen, J. A. Farrell, and M. Barth, "Real-time computer vision/DGPS-aided inertial navigation system for lane-level vehicle navigation," *IEEE Trans. Intell. Transp. Syst.*, vol. 13, no. 2, pp. 899–913, Jun. 2012.

[6] C. Thorpe, M. Hebert, T. Kanade, and S. Shafer, "Vision and navigation for the Carnegie-Mellon Navlab," *IEEE Trans. Pattern Anal. Mach. Intell.*, vol. 10, no. 3, pp. 362–373, May 1988.

[7] J. Li, J. Gao, H. Zhang, and T. Z. Qiu, "RSE-assisted lane-level positioning method for a connected vehicle environment," *IEEE Trans. Intell. Transp. Syst.*, vol. 20, no. 7, pp. 2644–2656, Jul. 2019.

[8] J. Baek, Y. Choi, C. Lee, J. Suh, and S. Lee, "BBUNS: Bluetooth beacon-based underground navigation system to support mine haulage operations," *Minerals*, vol. 7, no. 11, p. 228, Nov. 2017.

[9] X. Kong, X. Li, X. Song, Y. Tian, and D. Kong, "An accurate and reliable positioning methodology for land vehicles in tunnels based on UWB/INS integration," *Meas. Sci. Technol.*, vol. 33, no. 9, Jun. 2022, Art. no. 095107.

[10] P. J. Teunissen and O. Montenbruck, *Springer Handbook of Global Navigation Satellite Systems*, vol. 10. Cham, Switzerland: Springer, 2017.

[11] V. L. Knoop, P. F. de Bakker, C. C. J. M. Tiberius, and B. van Arem, "Lane determination with GPS precise point positioning," *IEEE Trans. Intell. Transp. Syst.*, vol. 18, no. 9, pp. 2503–2513, Sep. 2017.

[12] W. Hu, A. Neupane, and J. A. Farrell, "Using PPP information to implement a global real-time virtual network DGNSS approach," *IEEE Trans. Veh. Technol.*, vol. 71, no. 10, pp. 10337–10349, Oct. 2022.

[13] Y. Yuan, F. Shen, and X. Li, "GPS multipath and NLOS mitigation for relative positioning in urban environments," *Aerosp. Sci. Technol.*, vol. 107, Dec. 2020, Art. no. 106315.

[14] J. L. Weston and D. H. Titterton, "Modern inertial navigation technology and its application," *Electron. Commun. Eng. J.*, vol. 12, no. 2, pp. 49–64, Apr. 2000.

[15] X. Niu, S. Nassar, and N. El-Sheimy, "An accurate land-vehicle MEMS IMU/GPS navigation system using 3D auxiliary velocity updates," *Navigation*, vol. 54, no. 3, pp. 177–188, Sep. 2007.

[16] J. Farrell, *Aided Navigation: GPS With High Rate Sensors*, 1st ed. New York, NY, USA: McGraw-Hill, 2008.

[17] V. Pasku et al., "Magnetic field-based positioning systems," *IEEE Commun. Surveys Tuts.*, vol. 19, no. 3, pp. 2003–2017, 3rd Quart., 2017.

[18] J. Kuang, T. Li, Q. Chen, B. Zhou, and X. Niu, "Consumer-grade inertial measurement units enhanced indoor magnetic field matching positioning scheme," *IEEE Trans. Instrum. Meas.*, vol. 72, pp. 1–14, 2023.

[19] A. Canciani and J. Raquet, "Absolute positioning using the Earth's magnetic anomaly field," *Navigation*, vol. 63, no. 2, pp. 111–126, Jun. 2016.

[20] C. V. Kaji, R. C. Hoover, and S. Ragi, "Underwater navigation using geomagnetic field variations," in *Proc. IEEE Int. Conf. Electro Inf. Technol. (EIT)*, May 2019, pp. 1–6.

[21] P. Davidson and R. Piché, "A survey of selected indoor positioning methods for smartphones," *IEEE Commun. Surveys Tuts.*, vol. 19, no. 2, pp. 1347–1370, 2nd Quart., 2017.

[22] J. Kuang, X. Niu, P. Zhang, and X. Chen, "Indoor positioning based on pedestrian dead reckoning and magnetic field matching for smartphones," *Sensors*, vol. 18, no. 12, p. 4142, Nov. 2018.

[23] W. Team. (2020). *Global Positioning System Standard Positioning Service Performance Analysis Report*. [Online]. Available: https://www.nstb.tc.faa.gov/reports/2020Q4SPSPANv2.0.pdf

[24] P. Newson and J. Krumm, "Hidden Markov map matching through noise and sparseness," in *Proc. 17th ACM SIGSPATIAL Int. Conf. Adv. Geograph. Inf. Syst.*, 2009, pp. 336–343.

[25] A. Luo, S. Chen, and B. Xv, "Enhanced map-matching algorithm with a hidden Markov model for mobile phone positioning," *ISPRS Int. J. Geo-Inf.*, vol. 6, no. 11, p. 327, Oct. 2017.

[26] R. Toledo-Moreo, D. Betaille, and F. Peyret, "Lane-level integrity provision for navigation and map matching with GNSS, dead reckoning, and enhanced maps," *IEEE Trans. Intell. Transp. Syst.*, vol. 11, no. 1, pp. 100–112, Mar. 2010.

[27] C.-C. Wang et al., "MVP: Magnetic vehicular positioning system for GNSS-denied environments," in *Proc. 27th Annu. Int. Conf. Mobile Comput. Netw.* New York, NY, USA: Association for Computing Machinery, Oct. 2021, pp. 531–544.

[28] S. B. Cruz and A. Aguiar, "MagLand: Magnetic landmarks for road vehicle localization," *IEEE Trans. Veh. Technol.*, vol. 69, no. 4, pp. 3654–3667, Apr. 2020.

[29] P.-F. Ho, C.-C. Wang, and J.-C. Chen, "Using magnetic fingerprints to position cars on multi-layer roads," in *Proc. 26th Annu. Int. Conf. Mobile Comput. Netw.*, New York, NY, USA: Association for Computing Machinery, Sep. 2020, pp. 1–3.

[30] S. Jeon, H. Lee, and S. H. Son, “Poster: A magnetic fingerprint-based automobile position tracking using smartphones,” in *Proc. 14th Annu. Int. Conf. Mobile Syst., Appl., Services Companion*. New York, NY, USA: Association for Computing Machinery, 2016, p. 38.

[31] F. Li, P. Bonnifait, and J. Iba nez-Guzmán, “Map-aided dead-reckoning with lane-level maps and integrity monitoring,” *IEEE Trans. Intell. Vehicles*, vol. 3, no. 1, pp. 81–91, Mar. 2018.

[32] M. M. Atia et al., “A low-cost lane-determination system using GNSS/IMU fusion and HMM-based multistage map matching,” *IEEE Trans. Intell. Transp. Syst.*, vol. 18, no. 11, pp. 3027–3037, Nov. 2017.

[33] D. Wei, X. Ji, W. Li, H. Yuan, and Y. Xu, “Vehicle localization based on odometry assisted magnetic matching,” in *Proc. Int. Conf. Indoor Positioning Indoor Navigat. (IPIN)*, Sep. 2017, pp. 1–6.

[34] X. Ji, D. Wei, W. Li, Y. Lu, and H. Yuan, “A GM/DR integrated navigation scheme for road network application,” in *IPIN (Short Papers/Work-in-Progress Papers)*, 2019, pp. 117–124.

[35] J. Xinchun, W. Dongyan, Y. Hong, and Z. Deyun, “Vehicle multi-source fusion navigation method based on smartphone platform,” *J. Chin. Inertial Technol.*, vol. 28, no. 5, pp. 638–644, 2020.

[36] S. Liu et al., “Smartphone AHRS algorithm for vehicle based on magnetic interference compensation,” *Chin. J. Sensors Actuators*, vol. 35, no. 12, pp. 1643–1649, 2022.

[37] Y. Shu, C. Bo, G. Shen, C. Zhao, L. Li, and F. Zhao, “Magicol: Indoor localization using pervasive magnetic field and opportunistic WiFi sensing,” *IEEE J. Sel. Areas Commun.*, vol. 33, no. 7, pp. 1443–1457, Jul. 2015.

[38] Y. Wu, D. Zou, P. Liu, and W. Yu, “Dynamic magnetometer calibration and alignment to inertial sensors by Kalman filtering,” *IEEE Trans. Control Syst. Technol.*, vol. 26, no. 2, pp. 716–723, Mar. 2018.

[39] Y. Sakurai, M. Yoshikawa, and C. Faloutsos, “FTW: Fast similarity search under the time warping distance,” in *Proc. 24th ACM SIGMOD-SIGACT-SIGART Symp. Princ. Database Syst.* New York, NY, USA: Association for Computing Machinery, Jun. 2005, pp. 326–337.

[40] P. D. Groves, “Principles of GNSS, inertial, and multisensor integrated navigation systems, 2nd edition [book review],” *IEEE Aerosp. Electron. Syst. Mag.*, vol. 30, no. 2, pp. 26–27, Feb. 2015.

[41] E. H. Shin, “Estimation techniques for low-cost inertial navigation,” Ph.D. thesis, Dept. Geomatics Eng., Univ. Calgary, Calgary, ALB, Canada, 2005.

[42] L. Chang and K. Li, “Unified form for the robust Gaussian information filtering based on M-estimate,” *IEEE Signal Process. Lett.*, vol. 24, no. 4, pp. 412–416, Apr. 2017.

[43] Y. Yang, *Adaptive Navigation and Kinematic Positioning*. Beijing, China: Surveying and mapping press, 2006.

[44] J. Kuang, T. Li, and X. Niu, “Magnetometer bias insensitive magnetic field matching based on pedestrian dead reckoning for smartphone indoor positioning,” *IEEE Sensors J.*, vol. 22, no. 6, pp. 4790–4799, Mar. 2022.

Xiaoji Niu received the bachelor’s and Ph.D. degrees from the Department of Precision Instruments, Tsinghua University, in 1997 and 2002, respectively. He was a Post-Doctoral Research with the University of Calgary and a Senior Scientist with SiRF Technology Inc. He is currently a Professor with the GNSS Research Center, Wuhan University, China. He leads the Multi-Sensor Navigation Group (i2Nav) and focuses on GNSS/INS integrations, low-cost navigation sensor fusion, and its new applications. He has published more than 200 academic papers and owns more than 50 patents.

Longyang Ding received the B.E. degree (Hons.) in surveying and mapping engineering from Wuhan University, Wuhan, China, in 2022, where he is currently pursuing the M.S. degree in navigation, guidance and control with the GNSS Research Center. His research interests include GNSS/INS/magnetic-field integration for land vehicle navigation and mobile robot state estimation.

Yan Wang received the B.Eng. degree in chemical engineering and technology and the M.S. degree in computer applied technology from China University of Mining and Technology, Xuzhou, China, in 2016 and 2019, respectively. He is currently pursuing the Ph.D. degree with the GNSS Research Center, Wuhan University, Wuhan, China. His research interests include indoor navigation, sensor fusion algorithms, and computer vision.

Jian Kuang received the B.Eng. and Ph.D. degrees in geodesy and survey engineering from Wuhan University, Wuhan, China, in 2013 and 2019, respectively. He is currently an Associate Research Fellow with the GNSS Research Center, Wuhan University. His research interests include inertial navigation, pedestrian navigation, and indoor positioning.